Performance-Enhancement of Platform-Based, HF Direction-Finding Systems Using Dynamic Mode Selection

Kai Ren, *Member, IEEE,* Ruyu Ma, *Student Member, IEEE,* and Nader Behdad, *Fellow, IEEE,*

We present a method to enhance the accuracy of platform-based, high-frequency (HF) direction-finding (DF) systems using dynamic mode selection. To improve bandwidth and efficiency, the metallic platform supporting the DF array is used as the primary radiator by employing electrically small antennas to excite linearly independent combinations of its characteristic modes (CMs). However, the radiation characteristics of these modes vary dramatically over the HF band, making it difficult to achieve consistently good DF accuracy with a fixed system. To alleviate this, we propose a dynamic mode selection strategy to achieve enhanced DF accuracy. This strategy is based on the assumption that the number of available CMs of the platform is greater than the number of available coherent receive channels. Thus, dynamic mode selection allows for choosing the optimal antenna combination to obtain the best DF accuracy at each frequency. This strategy is demonstrated for an airborne DF system employing five electrically small antennas and up to four coherent receive channels. We demonstrate the efficacy of the proposed approach using computer simulations and scaled-model experiments. Simulation and measurement results show that dynamic mode selection can significantly enhance the DF accuracy of platform-based HF DF systems using a limited number of coherent receive channels.

Index Terms—**Aircraft antennas, characteristic mode (CM) theory, Cramer-Rao bound (CRB), direction of arrival (DoA) estimation, high frequency (HF) antennas, multiple signal classification (MUSIC) algorithm.**

I. INTRODUCTION

THE high-frequency (HF) band (3-30 MHz) is widely used in many military and some civilian applications. Examples include military communications, electronic warfare, and over the horizon radar systems as well as commercial radio broadcasting. Direction of arrival (DoA) estimation at this frequency range is of particular interest in many military applications. Various HF direction finding (DF) systems have been developed over the years. Examples include the Watson-Watt [1], pseudo-Doppler [2], phase interferometer [3], and Wullenweber DF systems [4]. In [1], two orthogonal Adcock antenna arrays were used in a Watson-Watt DF system with antenna lengths of approximately 10 m. In [2], a pseudo-Doppler DF system consisting of 8 antennas placed in a circular ring with a diameter of 100 m was reported. In the phase interferometer DF system reported in [3], the signal's DoA was estimated using spatially separated antennas with a distance of 122 m. In [4], a Wullenweber goniometer DF system was reported in which DF in the azimuth plane was performed using 120 monopoles located around the perimeter of a circle with a diameter of 291 m. In these examples, however, the dimensions of the DF arrays and the elements constituting them are physically large. As a result, these designs are not ideal candidates for mobile, HF DF applications.

Platform-based HF DF antennas have also been investigated over the years [5]-[8], [20]-[21]. In the 1940s and 1950s, platform-mounted HF DF antennas were designed without taking the presence of the platforms into account [5]-[7]. The optimal antennas' placement was studied by manually relocat-

ing them on different locations of naval and airborne platforms to reduce the impact of the platform on the performance of the DF array. However, the strong coupling between the antenna and the platform at the lower end of the HF band was a major problem [7]. With the aid of modern computational tools, the optimum placement of DF antennas was investigated with considering the platform [8]. To fully exploit the platform and reduce the coupling between the antenna and the platform, the theory of characteristic modes (CMs), developed in [9] and [10], has been applied to use the metallic platform supporting the antenna as the main radiator [11]-[22]. In [20]-[21], the CM theory was used to design various airplane-integrated HF DF antenna arrays. In [20], simulated radiation patterns of airborne HF antennas were utilized in the azimuth angle estimation based on the maximum likelihood algorithm. In [21], a systematic approach for designing platform-based HF DF arrays was proposed. In this work, the antennas mounted on the platform were used to excite a subset of the platform's CMs that can provide the best DF accuracy at a given frequency. However the DF performance of this fixed antenna array is not optimum at other frequencies. In [22], modal parameters and port specifications of a cubic antenna structure were investigated, where one or multiple ports were used to excite the pure CMs. Another practical challenge that many HF DF systems deal with is that their DF receivers usually have a limited number of coherent channels [23]. Thus, the performance of such practically constrained DF systems may still be improved if a dynamic mode selection approach is used. In such a scenario, the best combination of available antennas (or CMs) will be employed to perform DoA estimation. This allows for maintaining a consistent level of accuracy across the entire HF band.

In this paper, we present a method for improving the accuracy of a platform-based HF DF system that uses a receiver with a limited number of coherent receive channels. We assume that such a system uses electrically small antennas (ESA) to excite the characteristic modes of the platform and
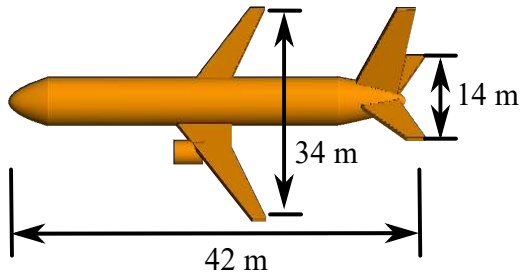
Fig. 1. Simplified model of the airplane used as the platform supporting the HF direction finding array examined in this work.
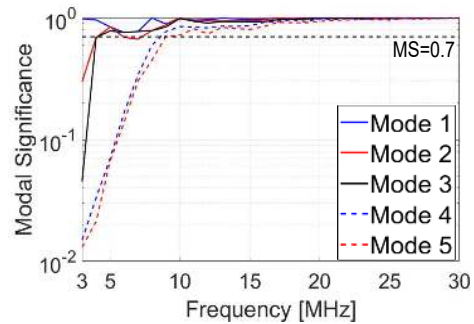

Fig. 2. Modal significance values of the first five modes of the simplified platform shown in Fig. 1 as a function of frequency.

that the number of ESAs used is greater than the number of available coherent receive channels. We demonstrate that dynamic mode selection in such a system can significantly improve the accuracy of the DF system across the entire HF frequency band. To the best of the authors' knowledge, dynamic mode selection to improve DF accuracy has not been investigated in the open literature. As a design example, an airborne DF system with five ESAs and a receiver having two to four coherent channels is examined. Furthermore, the ESAs mounted on the platform are designed to excite linearly independent combinations of the CMs of the platform rather than pure CMs. These two features are in contrast to the work presented in [21] in which a fixed number of coherent channels were used to perform DF and the antennas mounted on the platform were designed to purely excite individual CMs of the platform. The concepts proposed here can not only enhance the accuracy of a platform-based HF DF system but also simplify the design of the platform-based antennas and their feed networks. The performance of the full-scale platform-based DF system is evaluated using computer simulation tools and DF modeling techniques. These results show that using a dynamic mode selection algorithm, the DF accuracy of the system can be substantially improved across the entire HF band. In particular, the presented results show a marked performance improvement compared to the work presented in [21]. Furthermore, by using the antennas to excite linearly independent combinations of the CMs of the platform, the difficulties involved in implementing complex feed networks needed to excite pure CMs of the platform are entirely eliminated. A scaled-model prototype of the platform-based DF array was fabricated and was experimentally characterized using a near-field system. Using these measurement results, the DF performance of the fabricated scaled-model prototype were characterized in an emulated DF environment. The experimental results are found to be in good agreement with those obtained from the simulation-based studies and confirm the validity of the proposed approach.

II. THE CHARACTERISTIC MODES OF THE PLATFORM AND AVERAGE CRAMER-RAO BOUND

A. Characteristic Mode Analysis of a Medium-Size Aircraft

The model of the simplified medium-size aircraft considered in this work is shown in Fig. 1. CMs of the aircraft are investigated using the characteristic mode solver of the commercial software package FEKO [24]. Fig. 2 shows the modal significance (MS) values of the first five characteristic modes of the platform as a function of frequency. FEKO assigns mode numbers 1 to 5 according to the descending order of the MS values at the lowest frequency of 3 MHz and automatically tracks the modes across different frequencies. A mode is considered significant if its MS value is greater than 0.7. The MS value of a mode is an indicator of the efficiency with which it can be excited [10]. Observe that at the low end of the HF band (3 MHz) only a single significant mode exists. The number of significant modes increases as frequency increases. As a result, at the lower end of the HF band where the accuracy of any DF system with a fixed-size aperture is lowest, only a few modes can be efficiently used to perform direction finding. Therefore, in this work, we will only consider the first five CMs of the platform to design the proposed DF system. These five modes will provide a sufficiently high number of unique mode combinations (for 2-4 receive channels) to improve the DF accuracy by selecting suitable mode combinations as frequency or field of view is changed. Fig. 3 shows the normalized surface current distributions and radiation patterns of the first five CMs of the platform at 3, 4.25, 10, and 30 MHz. The observed differences in the CM radiation patterns and surface current distributions are caused by electrical size variations of the platform from 3 to 30 MHz. In FEKO, the CM numbers are assigned by the MS values. Fig. 3 shows that the current maxima occur on the wings and stabilizers of the aircraft and the current minima occur on the aircraft body and corners of the stabilizers. For example, for Mode 4 at 3 MHz, the current maxima occur on the horizontal and vertical stabilizers and the minima occur in the middle of the top of the aircraft's fuselage. To excite these modes, both inductive and capacitive coupling elements (ICEs and CCEs) may be employed. In doing so, ICEs should be placed at current maxima locations and CCEs should be placed at current minima locations [13]-[15].

B. Direction Finding Using the Characteristic Modes of the Platform

In this section, we examine the performance of a hypothetical DF system that uses different combinations of pure characteristic modes of the platform to estimate DoA of the
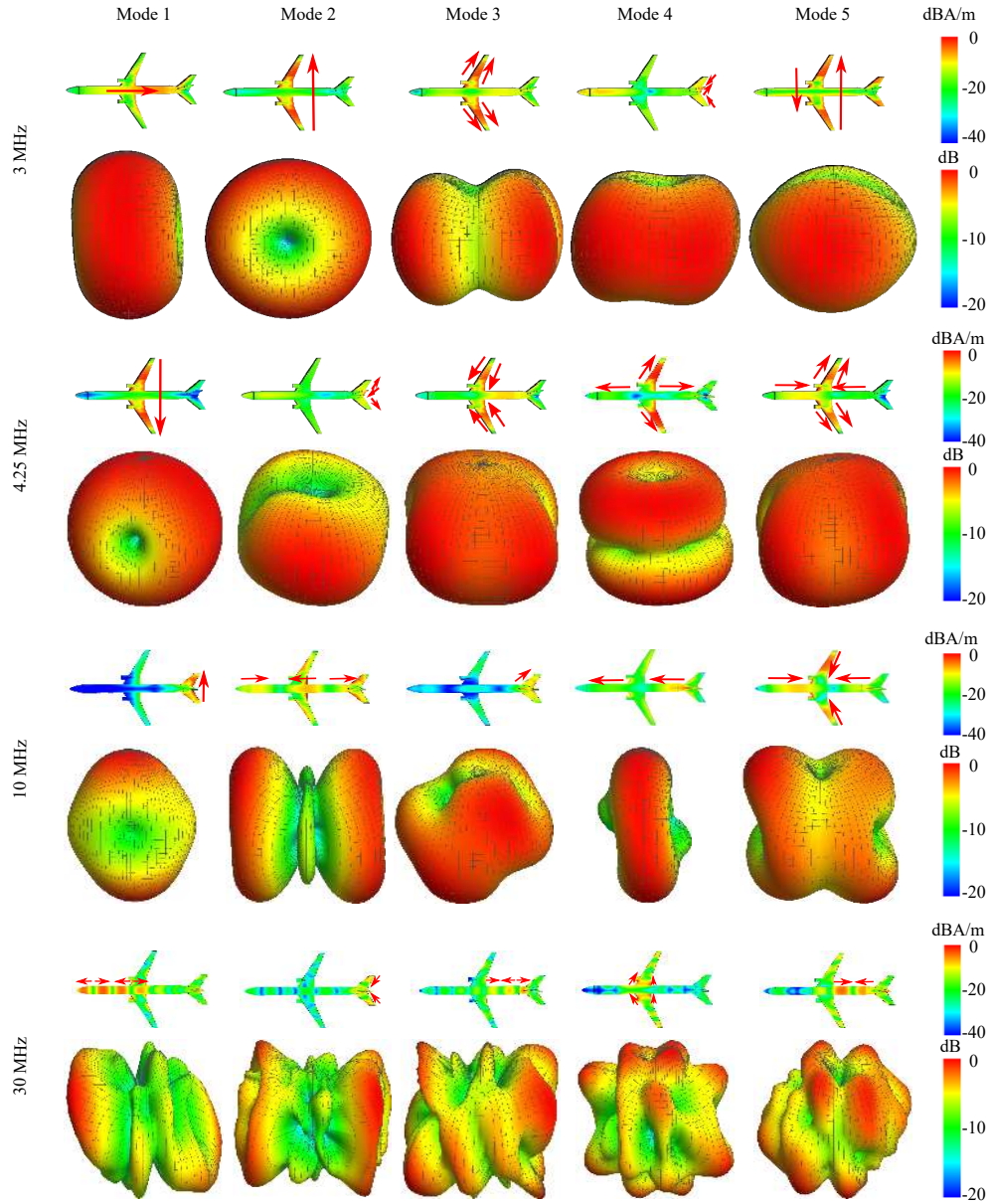
Fig. 3. Normalized surface current distributions and radiation patterns of the first five characteristic modes of the airborne platform shown in Fig. 1 at 3, 4.25, 10, and 30 MHz. The electric current flow directions are shown in red arrows.

signal. To quantify the accuracy of the DoA estimation and compare DF systems that use different combinations of the pure CMs of the platform, we use the Cramer-Rao bound (CRB) [25]. CRB provides a lower bound for the DoA estimation accuracy for this DF system. The setup of the problem considered in this section is shown in Fig. 4. Here, we assume that N uncorrelated signals having different directions of arrival (θ_n, ϕ_n) and polarizations, γ_n, illuminate the platform. Furthermore, we assume that the platform is oriented along the $\hat{x}$ direction (the nose of the platform coincides with the origin of the coordinate system). In this setup, $0° \leq \theta \leq 180°$ is the elevation angle, $0° \leq \phi < 360°$ is the azimuth angle, and the subscripts $n = 1 : N$ indicate the number of the source. Since the aircraft is in the far field of the sources, the incoming waves are assumed to be plane waves. A right-handed spherical coordinate system is formed by the unit vectors $\hat{\phi}, \hat{\theta}, -\hat{r}$. In the far field, the electric field intensity $\vec{E}_n$ for the nth source is in the $\hat{\phi} - \hat{\theta}$ plane and can be expressed by [25],

$$\vec{E}_n(t) = \hat{\phi}E_{n\phi}(t) + \hat{\theta}E_{n\theta}(t)$$
$$= a_n(t)e^{j\omega_0 t}[\hat{\phi}\sin(\gamma_n)e^{j\psi_n(t)} + \hat{\theta}\cos(\gamma_n)e^{j(\psi_n(t)+\eta_n)}] \quad (1)$$

where $a_n(t)$, ω_0, and $\psi_n(t)$ are the magnitude, angular frequency, and phase of the nth incoming wave at the given time t, respectively. The polarization tilt angle and the phase difference of the ϕ and θ components of the electric field ($\vec{E}_n$) are denoted by γ_n and η_n. It is assumed that the direction-finding array consists of M elements. Each antenna element
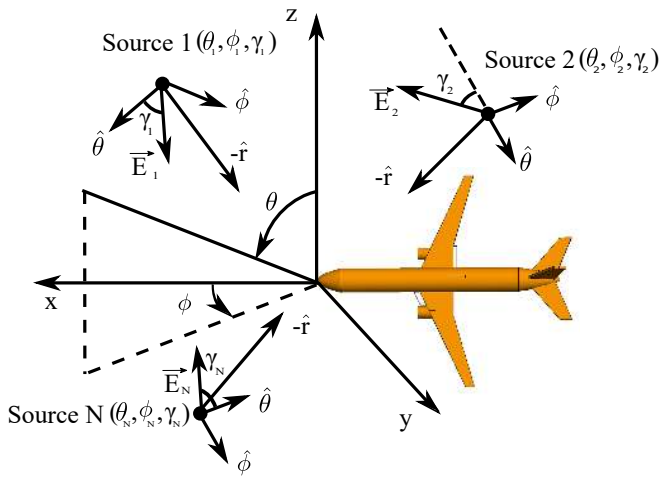
Fig. 4. The direction finding problem set up. The platform is oriented along the $\hat{x}$ direction with its nose placed at the center of the coordinate system. Multiple plane waves with directions of arrival of (θ_n, ϕ_n) and polarization states of γ_n propagate towards the DF array along the $-\hat{r}$ direction.

can have a different complex radiation pattern $(A_\phi(\theta, \phi), A_\theta(\theta, \phi))$. The voltages received by the antenna array can be expressed in the form of a matrix $\mathbf{X}(t)$ given by,

$$\mathbf{X}(t) = \mathbf{A}_\phi(\theta, \phi)\mathbf{E}_\phi(t) + \mathbf{A}_\theta(\theta, \phi)\mathbf{E}_\theta(t) + \mathbf{W}(t) \quad (2)$$

where $\mathbf{X}(t)$ is an $M \times 1$ column vector of voltages received by all M antenna elements at time $t = 1, 2, \ldots$; $\mathbf{A}_\phi$ and $\mathbf{A}_\theta$ are $M \times N$ matrices of ϕ, θ components of the complex radiation patterns; $\mathbf{E}_\phi(t)$ and $\mathbf{E}_\theta(t)$ are $N \times 1$ column vectors of the ϕ and θ components of electric fields of the N incoming waves; $\mathbf{W}(t)$ is an $M \times 1$ column vector of noise, which is assumed to be Gaussian white noise. The complex radiation patterns $\mathbf{A}_\phi$ and $\mathbf{A}_\theta$ can be obtained through full-wave electromagnetic simulations or measurements. Both techniques are employed in this paper to obtain the simulation and measurement results reported throughout the rest of the paper.

CRB is obtained by using the covariance of the matrix $\mathbf{X}$ in (2). A brief derivation for calculating the CRB values is shown in Appendix B and the detailed formulation is given in [25]. In this paper, the weighted average of the CRB matrix ($\mathbf{CRB}_{\text{avg}}$) [21] is used to quantify the performance of a given DF array,

$$\mathbf{CRB}_{\text{avg}} = \frac{\int d\gamma d\eta p(\gamma, \eta) \int_\Omega d\theta d\phi \cdot \mathbf{CRB}(\theta, \phi, \gamma, \eta) \sin\theta}{\Omega}$$
$$(3)$$

where $p(\gamma, \eta)$ is the independent and identically distributed probability density function of polarization states; Ω denotes the field of view (FoV); $\mathbf{CRB}(\theta, \phi, \gamma, \eta)$ is a function of DoAs (θ, ϕ) and incoming wave polarization γ, η (see Appendix B). In the rest of the paper, the focus will be on linearly-polarized waves (i.e., $\eta = 0$) and (θ, ϕ, γ) are estimated using the aforementioned process. Thus, $\mathbf{CRB}_{\text{avg}}$ is a 3×3 matrix, having $\theta\theta$ and $\phi\phi$ components $\text{CRB}_{\text{avg},\theta\theta}$ and $\text{CRB}_{\text{avg},\phi\phi}$ [1].

---

[1]These are two diagonal components of the matrix $\mathbf{CRB}_{\text{avg}}$.

To evaluate the DF performance on both elevation and azimuth angles, the scalar average CRB is introduced,

$$\text{CRB}_{\text{DoA}} = \text{CRB}_{\text{avg},\theta\theta} + \text{CRB}_{\text{avg},\phi\phi} \quad (4)$$

Note that $\sqrt{\text{CRB}_{\text{DoA}}}$ is used to quantify the DF accuracy of the system and has units of degrees. $\sqrt{\text{CRB}}$ is inversely proportional to the square root of the number of time samples collected and used in the DoA estimation algorithm ($\sqrt{K}$).

To estimate DoA of an emitter, a receiver which has at least two coherent channels is needed. When the number of the coherent channels of the receiver increases, the DF accuracy improves and the number of independent emitters that can be detected also increases. However, doing this adds to the cost and complexity of the system. Moreover, increasing the number of coherent receivers further complicates the calibration process of the DF system. As a result, most practical DF systems use only a few (i.e., between 2 to 4) coherent channels. In such situations, using a dynamic system that can intelligently select a subset of the available antennas to perform DoA estimation could be warranted. We will demonstrate this for the case of the platform-based DF system that uses the different combinations of pure CMs of the platform. In doing so, we assume that the first five modes of the platform are available for use in an idealized DF system and consider situations in which a DF receiver has between 2 and 4 receive channels.

C. Dynamic Mode Selection Using the Characteristic Modes of the Platform

To demonstrate the advantages of using dynamic mode selection, Fig. 5 shows the average CRB values calculated for this DF systems at four different frequencies within the HF band. The results are shown for three different cases of a system using a DF receiver with two, three, or four coherent channels. The CRB values calculated are averaged over the entire space (i.e., $0° \leq \theta \leq 180°, 0° \leq \phi < 360°$). The results show the average CRB value calculated using (3) and (4) with the complex CM radiation patterns obtained from CM analysis tool of FEKO v. 2017. In these calculations, one time snapshot of the signal (i.e., $K = 1$) and an available signal-to-noise ratio of SNR = 25 dB are used. The available SNR is defined as the ratio of the received signal power to the noise power assuming that the realized gain of the receiver antenna is 0 dBi. In using the CMs of the platform as the elements of the DF array, we assume that each CM corresponds to an antenna element with a total efficiency of 100% and a radiation pattern identical to that of its CM radiation pattern. The elevation angle θ is changed from $0°$ to $180°$ with a step size of $5°$ and the azimuth angle ϕ is changed from $0°$ to $360°$ with a step size of $5°$. Four linear polarization angles γ ($0°$, $30°$, $60°$, and $90°$) are assumed in this average CRB calculation. Note that $\sqrt{\text{CRB}}$ is inversely proportional to $\sqrt{K}$, indicating that the DF accuracy can be improved with increasing the snapshot number. In these results, however, we use a $K = 1$ to highlight the variations between the different cases, which allows for a better comparison of the results obtained from the different cases. As expected, a lower
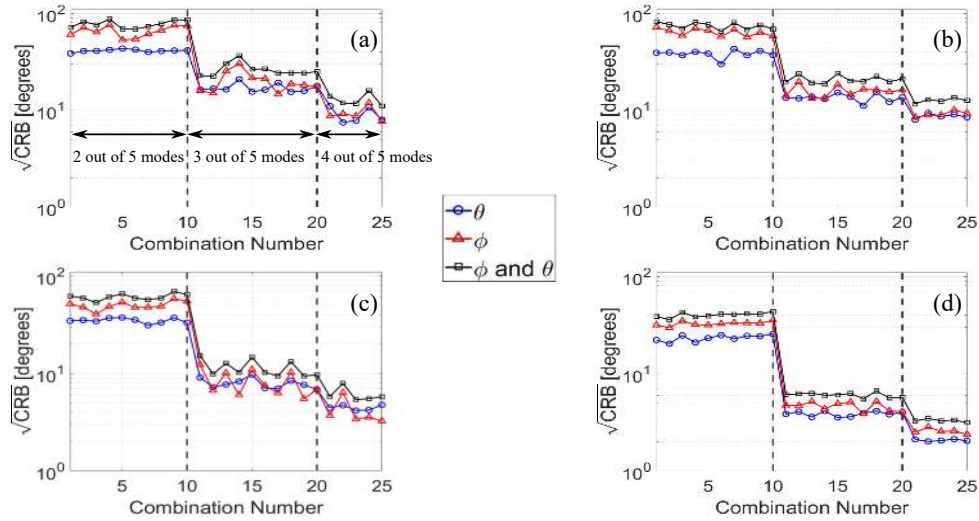
Fig. 5. The θ and ϕ components and the combined average $\sqrt{\mathrm{CRB}}$ over all FoV ($0° \leq \theta \leq 180°, 0° \leq \phi < 360°$) and the polarization angle ($0° \leq \gamma \leq 90°$) at different frequencies. (a) 3 MHz. (b) 4.25 MHz. (c) 10 MHz. (d) 30 MHz. The complex pure mode patterns of the aircraft shown in Fig. 3 are used. Two, three, and four out of five CMs are chosen. Blue lines show the average $\sqrt{\mathrm{CRB}_{\theta\theta}}$; red lines are the average $\sqrt{\mathrm{CRB}_{\phi\phi}}$; black lines are the $\theta\theta$ and $\phi\phi$ components combined $\sqrt{\mathrm{CRB}_{\mathrm{DoA}}}$. We assume the snapshot $K = 1$ and SNR = 25 dB. The first ten combinations (1-10 on the horizontal axis) use two modes; the following ten combinations (11-20 on the horizontal axis) use three modes; and the last five combinations (21-25 on the horizontal axis) use four modes. The detailed combinations of mode numbers are shown in Appendix A.

TABLE I
THE MINIMUM AVERAGE θ AND ϕ COMBINED $\sqrt{\mathrm{CRB}_{\mathrm{DoA}}}$ SUMMARIZED FROM FIG. 5 WHEN $K = 1$ AND SNR = 25 dB

Frequency [MHz]		3	4.25	10	30
Two CMs	Comb. No.	5	6	3	2
	$\sqrt{\mathrm{CRB}_{min}}$	68.7°	64.9°	53.0°	36.0°
Three CMs	Comb. No.	12	14	19	17
	$\sqrt{\mathrm{CRB}_{min}}$	22.5°	18.7°	9.4°	5.5°
Four CMs	Comb. No.	25	21	23	25
	$\sqrt{\mathrm{CRB}_{min}}$	11.1°	11.6°	5.4°	3.1°

average $\sqrt{\mathrm{CRB}}$ is obtained by using more receive channels. Moreover, the optimal combinations of the modes that offer the lowest CRB value does change as a function of frequency for a given number of available coherent channels. Therefore, it is necessary to develop a DF system supporting dynamic mode selection to achieve the optimal DF accuracy through the entire HF band. The optimal combination numbers and the modes included in each combination are listed in Appendix A (Table VII). In the results presented in Fig. 5, we show the CRB values averaged over all 4π Sr. field of view. This averaging process, smooths the natural variations that exist between the lower bound of DF accuracy of the different mode combinations at different directions. If the DoA of the wave is fixed, the different combinations of modes show a significantly wider variation of their CRB values even for cases where the same number of coherent receive channels are used. This larger variation makes the need for dynamic mode selection even more evident. However, considering the significant number of directions involved and the wide frequency range over which the present study is conducted, CRB values averaged over all fields of view are presented in in Fig. 5.

Table I shows the lowest average $\sqrt{\mathrm{CRB}}$ and the corresponding combination number at different frequencies. Ob-

serve that the optimal combination number resulting in the best achievable DoA accuracy is different at different frequencies. As Fig. 5 shows, when only two coherent channels are available, the accuracy of the DF system is lower compared to those of the other cases. In such a case, however, the accuracy can be increased by increasing the number of snapshots. A factor of 10 improvement can be obtained by increasing the number of samples from $K = 1$ to $K = 100$. Using only two coherent receive channels, however, has some other drawbacks, such as ambiguity in DoA estimation, that need to be taken into account. Furthermore, this system can only detect the DoA of a single signal. When the number of the receive channels is increased to three or four, the average $\sqrt{\mathrm{CRB}}$ is significantly lowered. As clearly demonstrated in this section, the optimum mode combination that results in the highest DoA estimation accuracy changes with frequency. Therefore, in a resource-constrained system where the number of coherent receive channels is less than the number of available antennas (or modes), using a dynamic mode selection mechanism may be warranted.

III. DESIGN EXAMPLE AND PRACTICAL IMPLEMENTATION ISSUES

In this section, we discuss the design of a platform-based antenna array designed to excite linearly independent combinations of the five characteristic modes of the platform examined in the last section. The DF capabilities of the array are simulated in situations where between two to four coherent receive channels are available to perform DF. In the simulations, the airplane model and electrically small coupling elements mounted on it are all assumed to be made of perfect electric conductors (PEC).

TABLE II
NORMALIZED COMPLEX WEIGHTING COEFFICIENTS OF THE CMs EXCITED BY EACH ANTENNA ELEMENT AT 3, 4.25, 10, AND 30 MHz

		Pure Mode				
		1	2	3	4	5
3 MHz	Ant. 1	$e^{-j11°}$	-	-	$0.22e^{j87°}$	$0.12e^{j89°}$
	Ant. 2	$e^{-j11°}$	$0.53e^{-108°}$	$0.16e^{j91°}$	$0.15e^{j87°}$	-
	Ant. 3	$0.15e^{j169°}$	-	-	$0.97e^{j87°}$	$e^{j89°}$
	Ant. 4	$0.26e^{-j11°}$	-	-	$0.28e^{-j93°}$	$e^{-j91°}$
	Ant. 5	$0.43e^{j169°}$	$e^{j72°}$	$0.27e^{j91°}$	$0.35e^{j87°}$	-
4.25 MHz	Ant. 1	$0.39e^{j175°}$	$0.61e^{-j92°}$	$e^{j120°}$	-	$0.82e^{j172°}$
	Ant. 2	$e^{j175°}$	-	$0.57e^{j120°}$	-	$0.29e^{j172°}$
	Ant. 3	$0.45e^{j175°}$	$0.91e^{-j92°}$	$0.19e^{j120°}$	$0.53e^{j89°}$	$e^{j172°}$
	Ant. 4	$0.26e^{j175°}$	$e^{j88°}$	$0.41e^{j120°}$	$0.24e^{j89°}$	$0.56e^{j172°}$
	Ant. 5	$0.2e^{-j5°}$	-	$0.24e^{j120°}$	-	$e^{j172°}$
10 MHz	Ant. 1	-	$e^{-j11°}$	$0.13e^{j135°}$	-	-
	Ant. 2	$e^{-j175°}$	-	$0.16e^{-j45°}$	$0.56e^{-j123°}$	$0.32e^{j79°}$
	Ant. 3	$0.74e^{j5°}$	$0.63e^{j169°}$	$0.42e^{j135°}$	-	$e^{j79°}$
	Ant. 4	$0.43e^{j5°}$	-	$0.68e^{j135°}$	-	$e^{-j101°}$
	Ant. 5	-	-	$0.62e^{j135°}$	$e^{j57°}$	$0.37e^{j79°}$
30 MHz	Ant. 1	$0.16e^{j178°}$	$0.48e^{j2°}$	$e^{-j174°}$	-	$0.49e^{-j10°}$
	Ant. 2	$0.36e^{j178°}$	$e^{j2°}$	$0.56e^{j6°}$	-	$0.16e^{j170°}$
	Ant. 3	$0.21e^{j178°}$	$0.19e^{-j178°}$	$0.4e^{j6°}$	$0.12e^{j178°}$	$e^{-j10°}$
	Ant. 4	$0.71e^{-j2°}$	$0.33e^{j2°}$	$0.45e^{-j174°}$	$0.17e^{-j2°}$	$e^{j170°}$
	Ant. 5	$0.47e^{j178°}$	$0.65e^{j2°}$	$0.28e^{j6°}$	$e^{-j2°}$	$0.61e^{j170°}$

TABLE III
EIGENVALUES OF THE COMPLEX WEIGHTING COEFFICIENTS SHOWN IN TABLE II

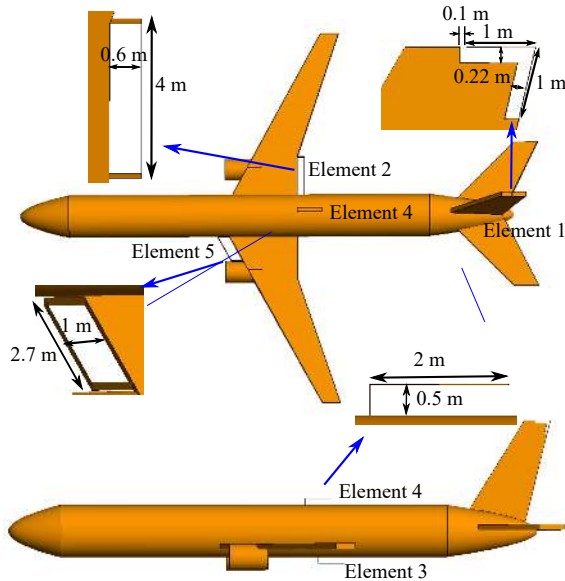| Frequency	Pure Mode				
	1	2	3	4	5
3 MHz	1	0.97	0.54	0.61	0.75
4.25 MHz	1	0.53	0.53	0.65	0.57
10 MHz	0.79	0.84	0.69	0.81	1
30 MHz	1	0.97	0.61	0.69	0.78

Fig. 6. The topology and dimensions of five coupling elements designed to excite linearly independent combinations of five CMs of the aircraft at 3 MHz. All coupling elements have the same width of 0.4 m.

A. Design of the Platform-Based Antenna Array

The CM currents and radiation patterns of the first five modes of the platform are shown in Fig. 3 at four different frequencies. To excite these modes, inductive and capacitive coupling elements will be used. ICEs (CCEs) should be located at locations on the platform where the density of the modal current is high (low) [13]-[15]. Moreover, excitation of the pure CM of the platform will usually require using more than a single coupling element. If designed properly, a single coupling element can be used to excite more than one CM. Fig. 3 shows that the edges of the wings, the vertical stabilizer, and the horizontal stabilizers are regions of high current density across the entire HF band. Hence, placement of ICEs at these locations can be used to efficiently excite the desired modes of the platform. Similarly, the corners of the horizontal and vertical stabilizers are locations of low current density (or high voltage intensity). Hence, placing CCEs at these locations is an effective method of exciting the desired CMs.

For the platform considered in this study, we have used five coupling elements to excite linearly independent combinations of the five characteristic modes of the aircraft, due to the orthogonality of pure CM modes. To reduce the complexity of the feeding network, these elements are excited individually. In determining the initial locations for mounting the coupling elements, the CM current distributions at 3 MHz were used as the primary guidance. This is due to the fact that at this frequency, only one mode is significant (i.e., has a modal significance value greater than 0.7) and can be readily excited. Other modes can still be excited but with a reduced bandwidth and efficiency compared to those of the dominant mode. The initial positions of Elements 1-5 were selected to be on the top of the vertical stabilizer, the back of the right wing, the middle of the bottom of the fuselage, the middle of the top of the fuselage, and the front of the left wing respectively. Then the design was optimized by changing the coupling elements'
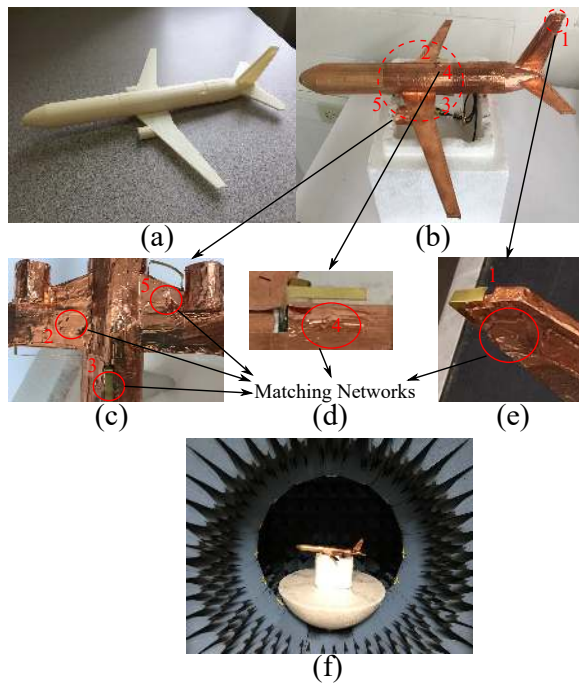
(a)　　　　　　(b)

(c)　　　　　(d)　　　　　(e)

→Matching Networks

(f)

Fig. 7. Photographs of (a) the 3D printed 1:100 scaled airplane model, (b) the fabricated prototype covered with copper tape, (c)-(e) antennas 1–5, and (f) the fabricated prototype placed in the multi-probe near-field measurement system. The buried passive matching networks are marked in solid red circles, which are connected the feed ports under the airplane using coaxial cables inside the aircraft's body.
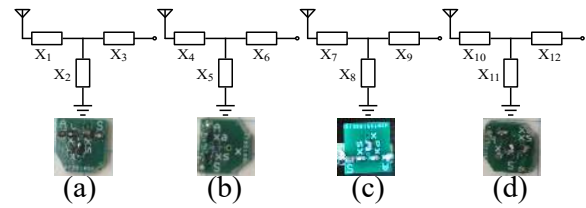

(a)　　　　(b)　　　　(c)　　　　(d)

Fig. 8. Topologies of the passive matching networks employed for the impedance matching of the coupling elements. (a) Element 1. (b) Element 2. (c) Elements 3 and 4. (d) Element 5. The presented fabricated matching networks on PCB are for the 1:100 scaled airplane at 3000 MHz (corresponding to the full model at 30 MHz).

TABLE IV
THE COMPONENT VALUES OF THE FABRICATED MATCHING NETWORK FOR THE 1:100 SCALED MODEL AT 425, 1000, AND 3000 MHz (CORRESPONDING TO 4.25, 10, 30 MHz FOR THE FULL-SCALE MODEL)

Frequency [MHz]	425	1000	3000
X_1	68 nH	Short	Short
X_2	36 nH	20 nH	0.6 pF
X_3	68 nH	36 nH	Short
X_4	3.3 pF	Short	1.5 pF
X_5	5.1 nH	0.5 pF	18 nH
X_6	Short	33 nH	1.2 nH
X_7	68 nH	Short	Short
X_8	39 nH	20 nH	0.7 pF
X_9	68 nH	43 nH	1.2 pF
X_{10}	3.3 pF	Short	Short
X_{11}	10 nH	18 nH	0.5 pF
X_{12}	Short	0.5 pF	1.8 pF

locations and examining absolute eigenvalues of the complex weighting coefficients of the excited antennas at 3 MHz. The weighting coefficients provide information about the number and the relative contributions of the modes excited by each antenna element. The coefficients were obtained using full-wave EM simulations in FEKO. If all five CMs are purely excited, the weighting coefficients will form a 5×5 identity matrix with eigenvalues of 1. If the CMs are not purely excited, the excited radiation patterns are linear combinations of the weighted CM patterns using the complex weighting coefficients. Therefore, the complex weighting coefficients of the CMs excited by each antenna element can be treated as a 5×5 transformation matrix $\mathbf{T}$ to transform the CM radiation patterns to the excited radiation patterns. Comparing the Fisher information matrix (FIM) elements shown in (12) and (13) in Appendix B, one can find that an extra noise term is added in the covariance matrix of the received signal if CMs are not purely excited. This extra noise is inversely proportional to the square of the eigenvalues of $\mathbf{T}$. Thus to maintain a desired performance level, a minimum acceptable threshold level for eigenvalues of $\mathbf{T}$ must be adopted. In this paper, we choose a threshold value of 0.5 for this purpose. However, other higher or lower threshold values may be selected depending on the requirements of the intended application. More details can be found in (10)-(13) in Appendix B.

Fig. 6 shows the final distribution of these different CEs across the platform, where the positions of Elements 1, 2, and 5 remain the same as the initial positions but the positions of Elements 3 and 4 are changed. Electrically small monopole antennas acting as CCEs are placed on the end of the vertical

stabilizer and top and bottom of the airplane, marked as Elements 1, 3, and 4. At these locations, the electric currents of Mode 4 at 3 MHz attain their minima allowing a CCE to efficiently excite these modes. Element 1 is designed to conform to the outer boundary of the vertical stabilizer. Elements 3 and 4 have the same dimensions. ICEs in the form of half loops are placed on the wings, where the current densities of Modes 1, 2, 3, and 5 at 3 MHz attain their maxima. These ICEs are labeled as Elements 2 and 5 in Fig. 6.

Table II shows the normalized complex weighting coefficients of the CMs excited by each antenna element, which form the 5×5 transformation matrix $\mathbf{T}$ at 3, 4.25, 10, and 30 MHz respectively. These results are obtained using full-wave EM simulations in FEKO assuming that the five coupling elements are excited individually across the entire HF band. The normalized complex weighting coefficients of higher-order CMs after the 5th CM are found to be insignificant. The coefficients with absolute values smaller than 0.1 are ignored in the table. Note that the radiated fields obtained from each set of excitation coefficients are a combination of multiple characteristic modes of the platform rather than a single CM. This is expected since excitation of a pure CM of the platform is rather challenging and often requires using numerous coupling elements distributed throughout the surface of the platform [15], [17]. This results in increasing the system complexity and may not offer any significant system level benefit in terms of enhancing the accuracy of the DF system. Table III presents the absolute eigenvalues of the 5×5 transformation matrix shown in Table II at different frequencies. Observe that the eigenvalues larger than 0.5 are
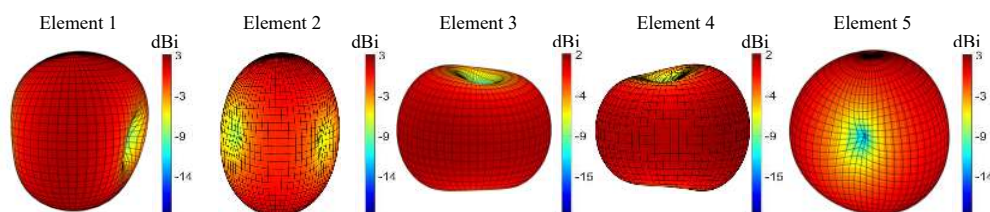
Fig. 9. The simulated radiation patterns of the full-scale aircraft-based antenna array at 3 MHz.
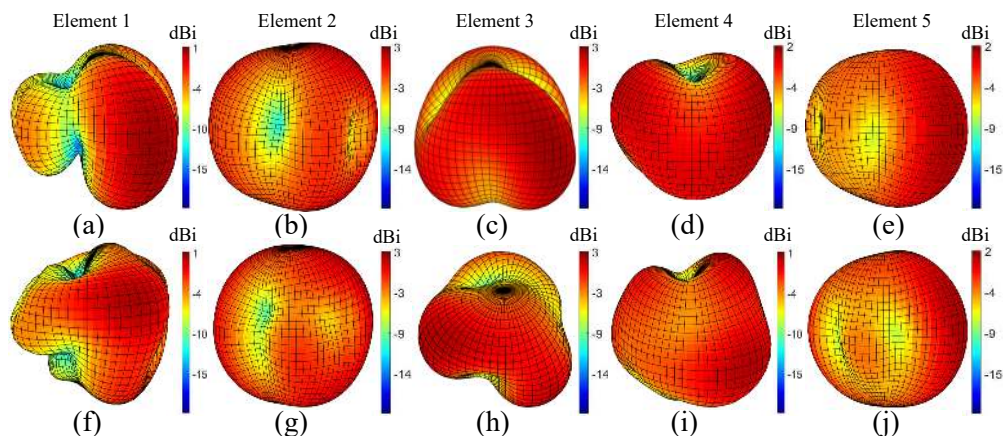

Fig. 10. The simulated and measured radiation patterns of the aircraft-based antenna array at 4.25 and 425 MHz. (a)-(e) show the simulated radiation patterns of the full-scale antenna array at 4.25 MHz, and (f)-(j) show the measured radiation patterns of the 1:100 scaled antenna array at 425 MHz.

achieved.

B. Fabrication of a 1:100 Scaled Model

Figs. 7(a) and 7(b) show the photographs of a 1:100 scaled model of the platform-based DF array examined earlier. The airplane model was 3-D printed from Acrylonitrile Butadiene Styrene (ABS) and covered with copper tape. The scaled CEs are made of brass with the dimensions shown in Fig. 6 scaled by a factor of 1:100. The PCBs shown in Fig. 8 are used to implement the impedance matching network for each coupling element (at each measurement frequency) and are embedded inside the scaled aircraft (shown in Figs. 7(c)-7(e)). The CEs are connected to the output sides of the matching networks. The inputs of the matching networks are connected to flexible coaxial cables, which go through the hollow airplane body and come out of the airplane's undercarriage. The five feeding ports are formed by soldering SMA connectors to the coaxial cables under the aircraft.

Fig. 8 shows the conventional three-element T-shaped matching networks, which are used to match the impedance of the CEs to 50 Ω [26]. ADS 2016 was employed for the matching network design, and Altium Designer was used for generating the PCB layouts. The PCBs were fabricated on FR4 substrates with dimensions of $10 \times 10 \times 1.6$ mm^3. To verify the proposed designs at different frequencies across the HF band, fixed matching networks for operation at 425, 1000, and 3000 MHz (corresponding to the full model at 4.25, 10 and 30 MHz in the HF band) were designed and fabricated. This allows for testing the performance of the platform-based DF array at three frequencies across the HF band. The component values of the fabricated networks are shown in Table IV. Photographs of

the fabricated impedance matching networks at 3000 MHz are shown in Fig. 8. These fixed impedance matching networks are used for convenience in the current experiments. In practice, the full-scale versions of such a DF system will use multi-channel HF receivers with automatic impedance tuners [27].

C. Comparison of the Simulated and Measured Radiation Patterns

The coherent (magnitude and phase), three-dimensional radiation pattern of each CE on the scaled airplane was measured using a near-field measurement system with the lowest frequency of operation of 425 MHz. The 1:100 scaled model was measured at 425, 1000, and 3000 MHz (corresponding to 4.25, 10, and 30 MHz of the full-scale model in the HF band). In both simulations and measurements, when one antenna element was excited, the other elements were terminated with a 50 Ω load. The simulated radiation patterns of the full-scale structure with element excitations at 3 MHz are shown in Fig. 9. Due to the limitation of the near-field radiation pattern measurement system, the fabricated prototype was not characterized at 300 MHz (corresponding to 3 MHz of the full-scale model).

In Figs. 10-12, the simulated radiation patterns of the full-scale prototype at 4.25, 10, and 30 MHz and the corresponding measured radiation patterns of the scaled prototype at 425, 1000, and 3000 MHz are presented. Qualitatively, most of the simulated and measured radiation patterns are similar to each other. The differences observed between the simulated and measurement results can primarily be attributed to the presence of the cables and connectors that protrude from the scaled-model platform and the realistic reactive elements used
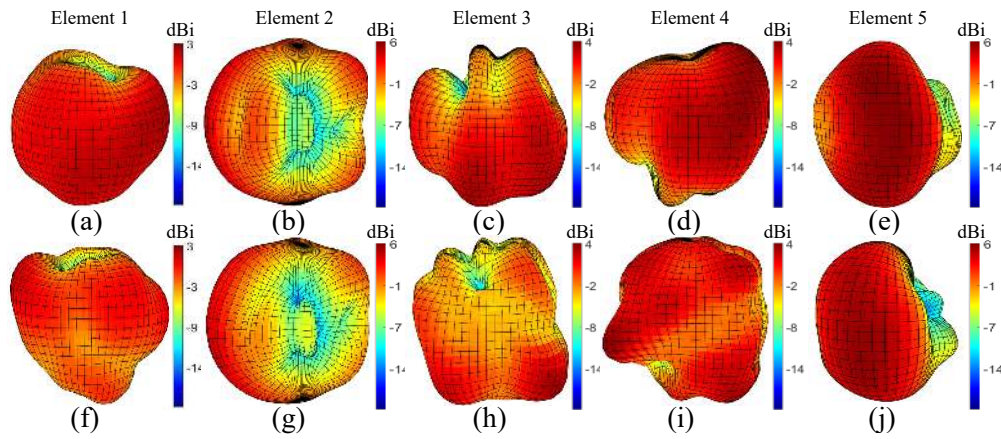
Fig. 11. The simulated and measured radiation patterns of the aircraft-based antenna array at 10 and 1000 MHz. (a)-(e) show the simulated radiation patterns of the full-scale antenna array at 10 MHz, and (f)-(j) show the measured radiation patterns of the 1:100 scaled antenna array at 1000 MHz.
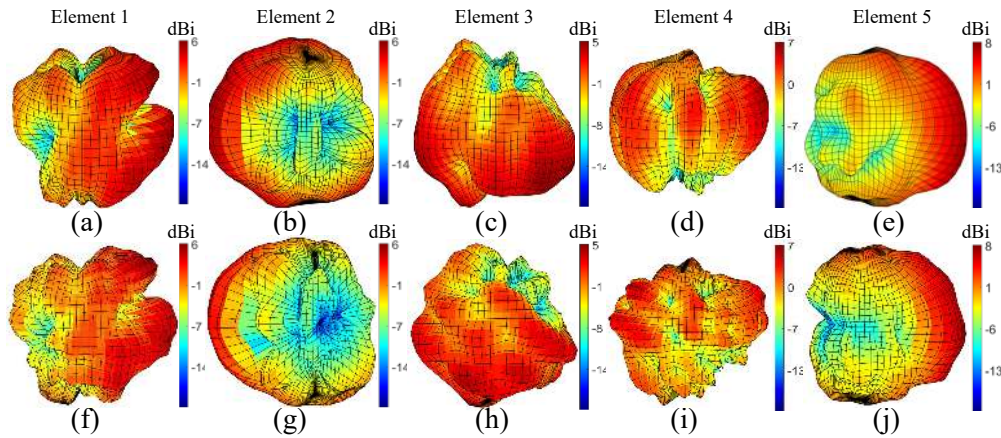

Fig. 12. The simulated and measured radiation patterns of the aircraft-based antenna array at 30 and 3000 MHz. (a)-(e) show the simulated radiation patterns of the full-scale antenna array at 30 MHz, and (f)-(j) show the measured radiation patterns of the 1:100 scaled antenna array at 3000 MHz.

in impedance matching, which do not exist in the full-scale model of the structure. The radiation efficiency of the antenna element 1 is approximately 50% at 425 MHz, 70% at 1 GHz, and 85% at 3GHz.

D. Dynamic Mode Selection Using the Platform-Based Antenna Array

To demonstrate the DF performance of the proposed platform-mounted antenna array using dynamic mode selection, two, three, and four out of five excited antennas were chosen to calculate CRB based on the simulated and measured complex-valued radiation patterns. Fig. 13 shows the simulated and measured average $\sqrt{\text{CRB}}$ at selected frequencies over all FoV. Comparing Figs. 13(a)-13(d), it is observed that a lower average $\sqrt{\text{CRB}}$ and a higher DoA accuracy can be achieved as the frequency increases. If a DF system has 3 coherent receive channels and a fixed combination number 16 (the optimal combination at 3 MHz) is used, the CRB values are $29°$, $24.4°$, $12.7°$, and $5.9°$ at 3, 4.25, 10, and 30 MHz, respectively based on these simulations. By using the dynamic mode selection, the DF accuracy, averaged over all FoV, could be improved by $1°$ (4%), $2.5°$ (20%), and $1.3°$ (22%) at 4.25, 10, and 30 MHz respectively. However, the results presented in Fig. 13

show CRB values averaged over all fields of view. Different combination of modes have different CRB values at different directions. Therefore, for a given direction of arrival of the wave, the variation between the CRB values corresponding to the different mode combinations is likely more significant than those observed in Fig. 13. There is a generally good agreement between the average $\sqrt{\text{CRB}}$ values calculated based on the simulated and those calculated based on measured radiation patterns. These CRB values are similar to those based on the CM patterns shown in Fig. 5. For example, the lowest $\sqrt{\text{CRB}}$ values are $10.2°$ and $9.5°$ using three simulated and fabricated antennas respectively at 10 MHz, which are close to $9.4°$ using three CMs. This good agreement demonstrates that the proposed antenna array provides a similar DF performance as the array using the pure CMs of the platform. These CRB values are obtained by assuming $K = 1$ and SNR = 25 dB. The CRB values will increase as SNR decreases. For situations where the SNR is low, the number of snapshots K needs to be increased to achieve acceptable accuracy.

Table V shows the minimum $\sqrt{\text{CRB}_{\text{DoA}}}$ in Fig. 13 calculated based on both simulated and measured radiation patterns. This table summarizes the best achievable DF accuracy using different number of antennas at different frequencies. Observe
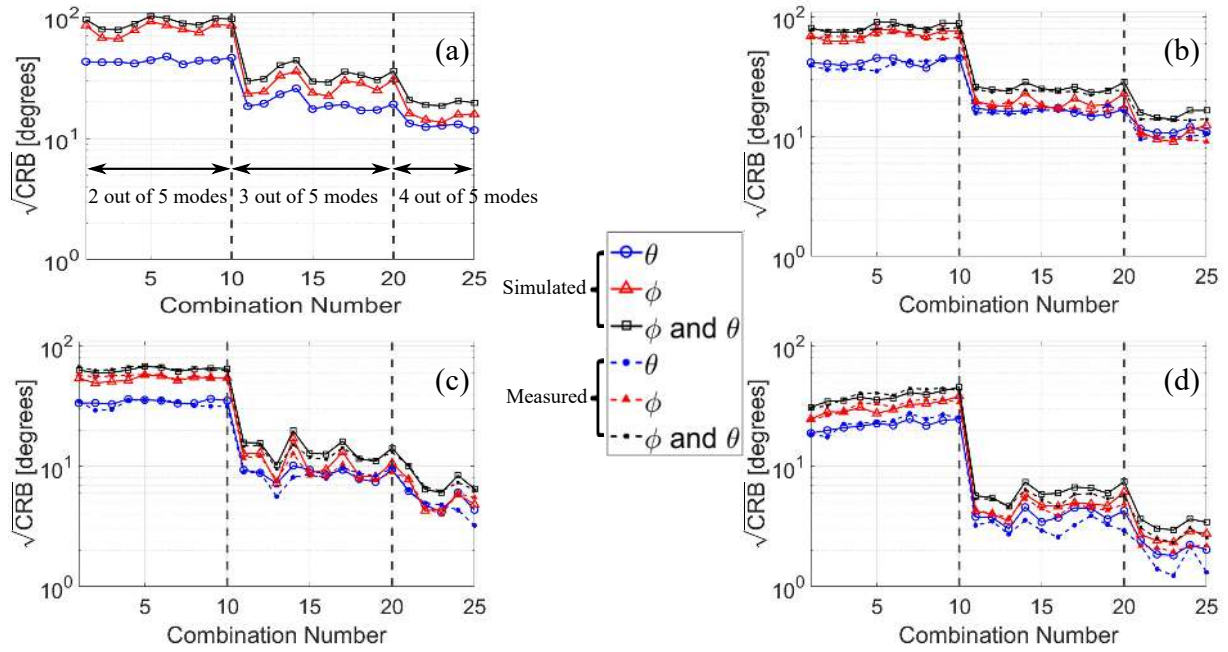
Fig. 13. The θ and ϕ components and the combined average $\sqrt{\text{CRB}}$ over all FoV ($0° \leq \theta \leq 180°, 0° \leq \phi < 360°$) and the polarization angle ($0° \leq \gamma \leq 90°$) at different frequencies. (a) 3 MHz. (b) 4.25 and 425 MHz. (c) 10 and 1000 MHz. (d) 30 and 3000 MHz. The complex simulated and measured radiation patterns of the aircraft shown in Fig. 9-12 are used. Two, three, and four out of five antennas are chosen. Blue lines show the average $\sqrt{\text{CRB}_{\theta\theta}}$; red lines are the average $\sqrt{\text{CRB}_{\phi\phi}}$; black lines are the $\theta\theta$ and $\phi\phi$ components combined $\sqrt{\text{CRB}_{\text{DoA}}}$. We assume the snapshot $K = 1$ and SNR $= 25$ dB.

TABLE V
THE COMPARISON BETWEEN THE SIMULATED AND MEASURED MINIMUM AVERAGE θ AND ϕ COMBINED $\sqrt{\text{CRB}_{\text{DoA}}}$ OVER ALL FoV WITH DIFFERENT NUMBER OF EXCITED ANTENNAS WHEN $K = 1$ AND SNR $= 25$ dB

Frequency [MHz]		3		4.25/425		10/1000		30/3000	
		Simulation	Measurement	Simulation	Measurement	Simulation	Measurement	Simulation	Measurement
Two Antennas	Comb. No.	3	-	3	3	2	2	1	1
	$\sqrt{\text{CRB}_{min}}$	78.9°	-	74.2°	77.6°	59.8°	62.6°	31.1°	30.7°
Three Antennas	Comb. No.	16	-	18	18	13	13	13	13
	$\sqrt{\text{CRB}_{min}}$	29.0°	-	23.4°	22.1°	10.2°	9.5°	4.6°	4.6°
Four Antennas	Comb. No.	23	-	23	23	23	23	23	23
	$\sqrt{\text{CRB}_{min}}$	18.6°	-	14.1°	13.8°	6.0°	6.2°	3.0°	2.3°

that, at each frequency, the measurements and simulations give similar minimum CRB values and the same antenna combinations in both cases provide this minimum value. Also, the change of the optimal antenna combination illustrates that by employing a dynamic mode selection approach, the DF accuracy as a function of frequency can be improved. When comparing the results presented in Table I with those reported in Table V, note that the optimal antenna combination numbers are different for the two cases. This is because in the first case pure CMs of the platform are used to perform direction finding and in the second case, the excited patterns, which are linearly independent combinations of different CMs, are used.

IV. DF PERFORMANCE OF THE AIRCRAFT-BASED ANTENNA ARRAY

To demonstrate the DF performance of the proposed aircraft-based antenna array, both the MUSIC algorithm and Monte Carlo test are used. The super-resolution MUSIC algorithm is widely used in DoA estimation, due to the advantages of reduced computational loads and lower sensitivity to the

white noise compared to other algorithms such as maximum likelihood and adapted angular response [28]. The noise subspace is obtained by eigenvalue decomposition of the covariance matrix of the received signals $\mathbf{R}_x = E(\mathbf{X}\mathbf{X}^H)$, where $\mathbf{X}$ is the received voltage in (2). The number of the noise eigenvectors Q is estimated by checking the number of normalized eigenvalues close to zero. The associated eigenvectors with these small eigenvalues form an $M \times Q$ noise subspace matrix $\mathbf{V}_Q$. Therefore, the MUSIC spectrum P_{MUSIC} with peaks showing the source parameters ($\theta_n, \phi_n, \gamma_n$) can be generated by [29],

$$\text{P}_{\text{MUSIC}}(\theta, \phi, \gamma) = \frac{1}{\mathbf{Y}^H(\theta, \phi, \gamma)\mathbf{V}_Q\mathbf{V}_Q^H\mathbf{Y}(\theta, \phi, \gamma)} \quad (5)$$

where the $M \times 1$ column vector $\mathbf{Y}(\theta, \phi, \gamma) = \mathbf{A}_\phi(\theta, \phi)\sin(\gamma) + \mathbf{A}_\theta(\theta, \phi)\cos(\gamma)$. The noise subspace matrix $\mathbf{V}_Q$ is orthogonal to the column vector $\mathbf{Y}(\theta_n, \phi_n, \gamma_n)$ only when the search of (θ, ϕ, γ) matches the nth source parameter ($\theta_n, \phi_n, \gamma_n$). By utilizing an M-element antenna array, the maximum detectable source number using the MUSIC algorithm is $N = M - 1$.

This article has been accepted for publication in a future issue of this journal, but has not been fully edited. Content may change prior to final publication. Citation information: DOI 10.1109/OJAP.2021.3095223, IEEE Open Journal of Antennas and Propagation

> REPLACE THIS LINE WITH YOUR PAPER IDENTIFICATION NUMBER <   11
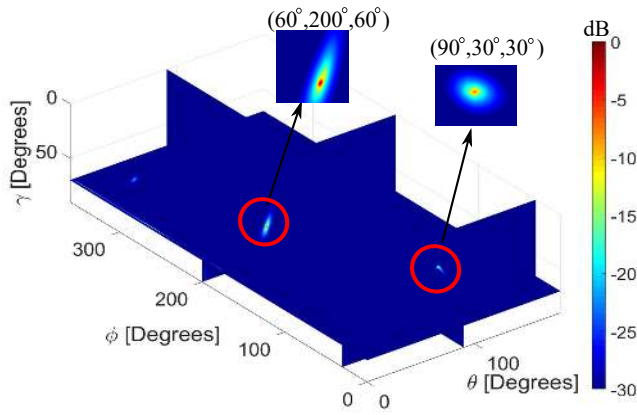
Fig. 14. The normalized MUSIC spectrum of DoA and polarization estimations of two uncorrelated sources. The measured complex radiation patterns of the 1:100 scaled prototype at 425 MHz are used. The dynamic range is 30 dB using the snapshot $K = 100$ and SNR = 25 dB.

TABLE VI
$\sqrt{\text{CRB}}$ AND MONTE CARLO TEST RESULTS OF THE TWO UNCORRELATED SOURCES WHEN $K = 100$ AND SNR = 25 dB

DoAs and Polarizations	Actual Values [°]	$\sqrt{\text{CRB}}$[°]	Estimated Values [°]	RMSEs [°]
θ_1/θ_2	90/60	0.15/0.28	90.01/59.99	0.17/0.32
ϕ_1/ϕ_2	30/200	0.49/0.40	29.91/199.98	0.61/0.44
γ_1/γ_2	30/60	0.18/0.35	30.04/59.94	0.27/0.69

Following the setup shown in Fig. 4, we assume that two uncorrelated sources with different DoAs and polarizations (θ, ϕ, γ): $(90°, 30°, 30°)$ and $(60°, 200°, 60°)$ illuminate the platform-based DF array at 4.25 MHz (425 MHz for the scaled model). Knowing from Table V that, the optimal combination 23 using the four excited antennas 1, 2, 4, and 5 offers the highest DF accuracy at this frequency, these antennas are used to perform DoA estimation based on the measured complex radiation patterns. The Monte Carlo test is performed in Matlab R2017a following this procedure,

1) Generate the received signals using (2) and add Gaussian white noise with SNR = 25 dB.
2) Apply the MUSIC algorithm (5) to estimate the DoA and polarization (θ, ϕ, γ).
3) Obtain the two sources parameters $(\theta_1, \phi_1, \gamma_1)$ and $(\theta_2, \phi_2, \gamma_2)$ by finding the first and second highest peaks in the MUSIC spectrum.
4) Repeat Steps 1 to 3 for 100 times and calculate the mean and root mean square error (RMSE) of θ, ϕ, and γ for each estimated source.

Fig. 14 shows an example of a MUSIC spectrum of the first numerical simulation in the Monte Carlo test, where the elevation angle θ is from $0°$ to $180°$ with step size of $1.25°$, the azimuth angle ϕ is from $0°$ to $360°$ with step size of $1.25°$, and the polarization angle γ is from $0°$ to $90°$ with step size of $0.5°$. Applying the measured complex radiation patterns of Elements 1, 2, 4, and 5 at 425 MHz to (5), the normalized 3-D MUSIC spectrum presents the accurate DoA and polarization estimations of the two uncorrelated sources without ambiguity with $K = 100$ and SNR = 25 dB. In

Fig. 14, the estimated DoAs and polarizations of the two sources marked in red circles and shown in zoomed images are the same as their actual DoAs and polarization angles $(90°, 30°, 30°)$ and $(60°, 200°, 60°)$, which would be slightly different in each simulation of the Monte Carlo test due to the random white Gaussian noise.

To further demonstrate the DF performance, Monte Carlo test was performed to obtain the mean values and RMSEs of the two sources' DoAs and polarization angles. As shown in Table VI, $(\theta_1, \phi_1, \gamma_1)$ and $(\theta_2, \phi_2, \gamma_2)$ denote the actual DoAs and polarization angles $(90°, 30°, 30°)$ and $(60°, 200°, 60°)$ of the two sources. Note that $\sqrt{\text{CRB}}$ here is for a given DoA (θ, ϕ) and polarization angle γ rather than the average over all FoV, which should be the lower bound of the DoA accuracy and smaller than RMSE. Each estimated value is the mean of the 100-time estimations of θ, ϕ, and γ. Table VI shows that both estimations are close to actual values and RMSEs approach $\sqrt{\text{CRB}}$, verifying the good DF performance of the proposed aircraft-based antenna array.

V. DISCUSSION

In this paper, we presented a method for enhancing the accuracy of platform-based HF direction finding systems that use DF receivers with a limited number of coherent channels. In such systems, it is feasible to use numerous, electrically small coupling elements to excite linearly independent combinations of the characteristic modes of the platform. Using these electrically small antennas as the elements of a DF array is analogous to using the pure CMs of the platform to perform direction finding. A large platform offers numerous significant modes that can be exploited for such a purpose. However, increasing the number of coherent receive channels at the same rate as increasing the number of antennas is often more challenging. We demonstrated that in such situations where the number of available modes is larger than that of the coherent receive channels, using a dynamic mode selection approach to perform DF task is warranted. Specifically, a design example for an airborne DF system using five ESAs and a receiver having between two and four coherent channels was presented. The Cramer-Rao bound was used to estimate the lower bound of the DoA accuracy of the system and determine the antenna combination that results in the best DoA accuracy at each frequency. We showed that this optimum antenna combination changes widely as a function of frequency. This suggests that a DF system that dynamically selects the optimum antenna combination for each frequency and expected FoV may be able to realize significant performance improvements over a static system such as the one reported in [21]. A 1:100 scaled-model prototype was fabricated and its DF performance was experimentally characterized. The results of the experimental studies corroborated those obtained from simulations and numerical modeling.

Finally, performing dynamic mode selection in a fielded system requires using a reconfigurable feed network. Such a feed network needs to be able to select M out of the available N antennas $(M < N)$ and can be implemented using a series of multi-port-multi-throw switches. The impedance matching

TABLE VII
COMBINATION NUMBERS USING TWO, THREE, AND FOUR OUT OF FIVE MODES (ANTENNAS)

Comb.	2 Modes (Antennas)	Comb.	3 Modes (Antennas)	Comb.	4 Modes (Antennas)
1	1, 2	11	1, 2, 3	21	1, 2, 3, 4
2	1, 3	12	1, 2, 4	22	1, 2, 3, 5
3	1, 4	13	1, 2, 5	23	1, 2, 4, 5
4	1, 5	14	1, 3, 4	24	1, 3, 4, 5
5	2, 3	15	1, 3, 5	25	2, 3, 4, 5
6	2, 4	16	1, 4, 5		
7	2, 5	17	2, 3, 4		
8	3, 4	18	2, 3, 5		
9	3, 5	19	2, 4, 5		
10	4, 5	20	3, 4, 5		

of the antennas can be performed using automatic impedance tuners, which are a common feature of many HF radios [27]. We envision that operation of a DF system using dynamic mode selection can be performed completely automatically. Any M antennas in the system can be used to scan the HF frequency band to detect signals of interest. Once such a signal is identified, the antenna combinations providing lowest CRB value at that frequency (averaged over all FoV) can be selected to perform an accurate DoA estimation. The process can be repeated as the monitored frequency changes.

APPENDIX A

The combination numbers are shown in Table VII. The combinations refer to the modes for the pure CMs and the antennas for the practical implementations. There are 10 combinations by choosing 2 out of 5 modes (antennas), 10 combinations by choosing 3 out of 5 modes (antennas), and 5 combinations by choosing 4 out of 5 modes (antennas).

APPENDIX B

For linearly-polarized waves (i.e., $\eta = 0$), $\mathbf{CRB}(\theta, \phi, \gamma)$ is obtained by the inverse of the Fisher information matrix (FIM) $\mathbf{F} = \{F_{pq}\}$ [25],

$$\mathbf{CRB}(\theta, \phi, \gamma) = \mathbf{F}^{-1} \quad (6)$$

where each element in FIM, F_{pq}, is denoted by,

$$F_{pq} = K \cdot \mathrm{tr} \left\{ \mathbf{R}_x^{-1} \frac{\partial \mathbf{R}_x}{\partial p} \mathbf{R}_x^{-1} \frac{\partial \mathbf{R}_x}{\partial q} \right\} \quad (7)$$

where K is the time sample of the received signal, $\mathrm{tr}\{\cdot\}$ denotes the trace operation of a matrix, the parameter vectors p and q denote θ, ϕ, or γ, and the $M \times M$ covariance matrix $\mathbf{R}_x$ of the received signal $\mathbf{X}$ is,

$$\mathbf{R}_x = \mathbf{A}\mathbf{R}_s\mathbf{A}^H + \sigma^2 \mathbf{I} \quad (8)$$

where the $M \times 2N$ matrix $\mathbf{A} = [\mathbf{A}_\theta, \mathbf{A}_\phi]$ represents the pure CM or excited antenna radiation patterns respectively and $\mathbf{R}_s = \mathbf{S}\mathbf{S}^H$ is a $2N \times 2N$ covariance matrix of a signal with a $2N \times 1$ matrix $\mathbf{S} = [\mathbf{E}_\phi, \mathbf{E}_\theta]^T$. Note that T represents the transpose operator and H is the Hermitian operator, which is the complex conjugate transpose. $\sigma^2 \mathbf{I}$ is the variance matrix of Gaussian white noise and $\mathbf{I}$ is the identity matrix.

Dividing both sides of (8) by σ^2, $\mathbf{R} = \mathbf{A}\mathbf{P}\mathbf{A}^H + \mathbf{I}$ is obtained with $\mathbf{P} = \mathbf{R}_s/\sigma^2$ for convenience to express the following equation. Substituting $\mathbf{R}$ into (7), a simplified FIM element is achieved without the trace operation,

$$\begin{aligned} F_{pq} = 2K \cdot \mathrm{Re} \Big\{ &(\mathbf{P}\mathbf{A}^H \mathbf{R}^{-1} \mathbf{A}\mathbf{P}) \times (\dot{\mathbf{A}}_q^H \mathbf{R}^{-1} \dot{\mathbf{A}}_p)^T \\ &+ (\mathbf{P}\mathbf{A}^H \mathbf{R}^{-1} \dot{\mathbf{A}}_q) \times (\mathbf{P}\mathbf{A}^H \mathbf{R}^{-1} \dot{\mathbf{A}}_p^H)^T \Big\} \end{aligned} \quad (9)$$

where $\dot{\mathbf{A}}_p$ ($\dot{\mathbf{A}}_q$) denotes the partial derivative of $\mathbf{A}$ with respect to p (q).

With knowing the CRB formulation, the following derivations aim to find the relation between CRB values based on the CM and excited antenna patterns, which is equivalent to finding the relation between the two FIM elements. The pure CM pattern matrix is assumed to be $\mathbf{B}$. Because the coupling elements excite a linearly independent combination of CMs, the excited pattern matrix is written as $\mathbf{C} = \mathbf{T}\mathbf{B}$, where the transformation matrix is $\mathbf{T} = \mathbf{U}\boldsymbol{\Lambda}\mathbf{U}^H$ with the eigenvector matrix $\mathbf{U}$ and diagonal eigenvalue matrix $\boldsymbol{\Lambda}$. Substituting $\mathbf{B}$ and $\mathbf{C} = \mathbf{T}\mathbf{B}$ into (8), the covariance matrices $\mathbf{R}_b$ and $\mathbf{R}_c$ are given by,

$$\mathbf{R}_b = \mathbf{B}\mathbf{P}\mathbf{B}^H + \mathbf{I} \quad (10)$$

$$\mathbf{R}_c = \mathbf{T} \cdot [\mathbf{B}\mathbf{P}\mathbf{B}^H + \mathbf{U}(\boldsymbol{\Lambda}^H \boldsymbol{\Lambda})^{-1} \mathbf{U}^H] \cdot \mathbf{T}^H \quad (11)$$

Rewriting (9) based on (10), the FIM element for the CM patterns becomes,

$$\begin{aligned} F_{pq}^b = 2K \cdot \mathrm{Re} \Big\{ &(\mathbf{P}\mathbf{B}^H \mathbf{R}_b^{-1} \mathbf{B}\mathbf{P}) \times (\dot{\mathbf{B}}_q^H \mathbf{R}_b^{-1} \dot{\mathbf{B}}_p)^T \\ &+ (\mathbf{P}\mathbf{B}^H \mathbf{R}_b^{-1} \dot{\mathbf{B}}_q) \times (\mathbf{P}\mathbf{B}^H \mathbf{R}_b^{-1} \dot{\mathbf{B}}_p^H)^T \Big\} \end{aligned} \quad (12)$$

Similarly rewriting (9) based on (11) and using $\mathbf{C} = \mathbf{T}\mathbf{B}$, the FIM element for the excited patterns becomes,

$$\begin{aligned} F_{pq}^c = 2K \cdot \mathrm{Re} \Big\{ &(\mathbf{P}\mathbf{B}^H \tilde{\mathbf{R}}_c^{-1} \mathbf{B}\mathbf{P}) \times (\dot{\mathbf{B}}_q^H \tilde{\mathbf{R}}_c^{-1} \dot{\mathbf{B}}_p)^T \\ &+ (\mathbf{P}\mathbf{B}^H \tilde{\mathbf{R}}_c^{-1} \dot{\mathbf{B}}_q) \times (\mathbf{P}\mathbf{B}^H \tilde{\mathbf{R}}_c^{-1} \dot{\mathbf{B}}_p^H)^T \Big\} \end{aligned} \quad (13)$$

where $\tilde{\mathbf{R}}_c = \mathbf{B}\mathbf{P}\mathbf{B}^H + \mathbf{U}(\boldsymbol{\Lambda}^H \boldsymbol{\Lambda})^{-1} \mathbf{U}^H$, which is different from $\mathbf{R}_c$ in (11). Compared with the FIM elements (12) and (13), the only difference between using the CM and excited patterns is in the covariance matrices $\mathbf{R}_b$ and $\tilde{\mathbf{R}}_c$. For these two matrices, the first terms $\mathbf{B}\mathbf{P}\mathbf{B}^H$ are the same and the second terms $\mathbf{I}$ and $\mathbf{U}(\boldsymbol{\Lambda}^H \boldsymbol{\Lambda})^{-1} \mathbf{U}^H$ are different. If the CMs are not purely excited, the eigenvalue matrix $\boldsymbol{\Lambda}$ has diagonal values smaller than 1. This indicates that extra noise is added. Therefore, a minimum threshold on the acceptable eigenvalues of this matrix must be set. In this paper, we set this value to be 0.5.

REFERENCES

[1] R. A. Watson Watt and J. F. Herd, "An instantaneous direct-reading radiogoniometer," *IEE*, vol. 1, no. 2, pp. 89-95, Jun. 1926.
[2] C. W. Earp and R. M. Godfrey, "Radio direction-finding by the cyclical differential measurement of phase," *J. IEE*, vol. 94, pt. IIIA, pp. 705–721, Apr. 1947.
[3] C. W. McLeish and N. Burtnyk, "The application of the interferometer to HF direction finding," *Proc. IEE*, vol. 108, no. 41, pp. 495-499, Sep. 1961.
[4] P. J. D. Gething, "High-frequency direction finding," *Proc. IEE*, vol. 113, no. 1, pp. 49–61, Jan. 1966.

[5] C. Crampton, "Naval radio direction-finding," *J. IEE*, vol. 94, no. 11, pp. 132-153, Mar. 1947.

[6] M. K. Goldstein and J. W. Green, "Flight investigation of suitable HF-DF collector locations on PV-1 navy patrol bomber," *Naval Res. Lab. Rep.*, No. R-2469, Feb. 1945.

[7] P. S. Carter, "Study of the feasibility of airborne HF direction-finding antenna systems," *IRE Trans. Aeronaut. Navig. Electron.*, vol. ANE-4, No. 1, pp. 19–23, Mar. 1957.

[8] G. Byun, H. Choo, and H. Ling, "Optimum placement of DF antenna elements for accurate DoA estimation in a hash platform environment," *IEEE Trans. Antennas Propag.*, vol. 61, no. 9, pp. 4783–4791, Sep. 2013.

[9] R. Garbacz and R. Turpin, "A generalized expansion for radiated and scattered fields," *IEEE Trans. Antennas Propag.*, vol. AP-19, no. 3, pp. 348–358, May 1971.

[10] R. Harrington and J. Mautz, "Theory of characteristic modes for conducting bodies," *IEEE Trans. Antennas Propag.*, vol. AP-19, no. 5, pp. 622–628, Sep. 1971.

[11] K. Obeidat, R. G. Rojas, and B. Raines, "Design of antenna conformal to V-shaped tail of UAV based on the method of characteristic modes," *Proc. 3rd Eur. Conf. Antennas Propag.*, pp. 2493–2496, 2009.

[12] Y. Chen and C.-F. Wang, "Electrically small UAV antenna design using characteristic modes," *IEEE Trans. Antennas Propag.*, vol. 62, no. 2, pp. 535–545, Feb. 2014.

[13] Y. Chen and C.-F. Wang, *Characteristic Modes: Theory and Applications in Antenna Engineering*. Hoboken, NJ: John Wiley & Sons, 2015.

[14] Y. Chen and C.-F. Wang, "HF band shipboard antenna design using characteristic modes," *IEEE Trans. Antennas Propag.*, vol. 63, no. 3, pp. 1004-1013, Mar. 2015.

[15] T.-Y. Shih and N. Behdad, "Bandwidth enhancement of platform-mounted HF antennas using the characteristic mode theory," *IEEE Trans. Antennas Propag.*, vol. 64, no. 7, pp. 2648-2659, Jul. 2016.

[16] M. Li and N. Behdad, "Dual-band platform-mounted HF/VHF antenna design using the characteristic mode theory," *IET Microw. Antennas Propag.*, vol. 12, no. 4, pp. 452-458, Mar. 2018.

[17] R. Ma, T.-Y. Shih, R. Lian, and N. Behdad, "Design of bandwidth-enhanced, platform-mounted, electrically small VHF antennas using the characteristic-mode theory," *Antennas Wireless Propag. Lett.*, vol. 17, no. 12, pp. 2384-2388, Dec. 2018.

[18] K. Ren, M. R. Nikkhah, and N. Behdad, "Earth effect emulation using periodic structures in scaled-model characterization of HF antennas," *IEEE Antennas Wireless Propag. Lett.*, vol. 18, no. 12, pp. 2731-2735, Dec. 2019.

[19] K. Ren*, M. R. Nikkhah*, and N. Behdad, "Design of dual-polarized, platform-based HF antennas using the characteristic mode theory," *IEEE Trans. Antennas Propag.*, vol. 68, no. 7, pp. 5130–5141, Jul. 2020.

[20] C. F. Corbin, "High frequency direction finding using structurally integrated antennas on a large airborne platform," M. S. thesis, Air Force Institute of Technology, Wright-Patterson Air Force Base, OH, 2011.

[21] R. Ma and N. Behdad, "Design of platform-based HF direction-finding antennas using the characteristic mode theory," *IEEE Trans. Antennas Propag.*, vol. 67, no. 3, pp. 1417–1427, Mar. 2019.

[22] L. Grundmann, N. Peitzmeier, and D. Manteuffel, "Investigation of direction of arrival estimation using characteristic modes'," *15th Eur. Conf. Antennas Propag.*, pp. 1–5 Mar. 2021.

[23] W. Read, "Review of conventional tactical radio direction finding systems," *Defence Res. Establishment Ottawa Tech. Note*, May, 1989.

[24] FEKO Altair Engineering Inc., [online] Available: https://www.altair.com/feko/.

[25] A. J. Weiss and B. Friedlander, "Performance analysis of diversely polarized antenna arrays," *IEEE Trans. signal process.*, vol. 39, no. 7, pp. 1589-1603, Jul. 1991.

[26] C. Bowick, *RF Circuit Design*. Burlington, MA: Newnes, 1982.

[27] Palstar. HF-automatic antenna tuner, [Online] Available: http://www.palstar.com/en/hf-auto/.

[28] E. Ferrara and T. Parks, "Direction finding with an array of antennas having diverse polarizations," *IEEE Trans. Antennas Propag.*, vol. 31, no. 2, pp. 231-236, Mar. 1983.

[29] R. Schmidt, "Multiple emitter location and signal parameter estimation," *IEEE Trans. Antennas Propag.*, vol. 34, no. 3, pp. 276-280, Mar. 1986.

Kai Ren (S'14–M'18) received the B. S. and M. S. degrees in Electrical Engineering from Xidian University, Xi'an, China, in 2010 and 2013, respectively, and the Ph. D. degree in Electrical and Computer Engineering from the Ohio State University, Columbus in 2017.

Dr. Ren is currently an Assistant Professor in the Department of Electrical and Computer Engineering, Wentworth Institute of Technology, Boston, MA, USA. From 2018 to 2020, he was a Postdoctoral Research Fellow in the Department of Electrical and Computer Engineering, University of Wisconsin-Madison, Madison, WI, USA. His current research includes platform-based antennas, electrically small antennas, characteristic mode theory, direction finding systems, scattering problems and microwave imaging, and radar signal processing.

Ruyu Ma received the Ph.D. degree in Electrical Engineering from the University of Wisconsin-Madison in 2020. His research interests include direction-of-arrival (DoA) estimation, electrically small antenna arrays and platform-based antennas. He was the recipient of the 2nd award of student paper competition at USNC/URSI National Radio Science Meeting (2020). He is a Student Member of the IEEE.

Nader Behdad (S'98-M'06–SM'12–F'17) received the B.S. degree in Electrical Engineering from Sharif University of Technology in 2000 and the M.S. and Ph.D. degrees in Electrical Engineering from University of Michigan - Ann Arbor in 2003 and 2006, respectively. Currently he is the McFarland-Bascom Professor in the Department of Electrical and Computer Engineering of the University of Wisconsin-Madison. Dr. Behdad's research expertise is in the area of applied electromagnetics with particular focus on electrically small antennas, phased-array antennas, bio-electromagnetics, microwave ablation, microwave periodic structures, and high-power microwaves. He has 21 issued or pending U.S. patents in these areas. Dr. Behdad has served as a consultant on topics related to designing antennas and phased arrays to industry. He has also served as a consultant and an expert witness for different U.S. law firms on topics related to intellectual property disputes as well as cell phone record analysis and historical cell site analysis. Over the years, Dr. Behdad's research has been sponsored by various U.S. Federal agencies including the U.S. Navy, U.S. Air Force, U.S. Army, National Science Foundation, and the Defense Health Agency.

Dr. Behdad is the recipient of the Harvey D. Spangler Faculty Scholar Award, the H. I. Romnes Faculty Award, and the Vilas Associates Award from the University of Wisconsin-Madison. He received the 2014 R. W. P. King Prize Paper Award, and the 2012 Piergiorgio L. E. Uslenghi Letters Prize Paper Award of the IEEE Antennas and Propagation Society. In 2011, he received the CAREER award from the U.S. National Science Foundation, the Young Investigator Award from the United States Air Force Office of Scientific Research, and the Young Investigator Award from the United States Office of Naval Research. Dr. Behdad served as the 2020 chair of the paper awards committee of the IEEE Antennas and Propagation Society. He also served as an Associate Editor for IEEE Antennas and Wireless Propagation Letters (2011-2015) and as the co-chair of the technical program committee of the 2012 IEEE International Symposium on Antennas and Propagation and USNC/URSI National Radio Science Meeting.